Chemical Engineering Science 290 (2024) 119909

Contents lists available at ScienceDirect

Chemical Engineering Science

journal homepage: www.elsevier.com/locate/ces

A filtering approach for applying the two-fluid model to gas-liquid flows on high resolution grids

Benjamin Krull [a,*], Richard Meller [a], Matej Tekavčič [b], Fabian Schlegel [a]

[a] Institute of Fluid Dynamics, Helmholtz-Zentrum Dresden–Rossendorf, Bautzner Landstr. 400, 01328 Dresden, Germany
[b] Reactor Engineering Division, Jožef Stefan Institute, Jamova cesta 39, 1000 Ljubljana, Slovenia

ARTICLE INFO

Keywords:
Multi-phase flows
Two-phase flow
Two-fluid model
Euler-Euler
Mesh dependence
Filtering
Diffusion
Finite volume method
Bubbles
OpenFOAM
Morphology-adaptive methods

ABSTRACT

The two-fluid model is usually combined with closure forces designed for applications on coarse grids, i.e. bubbles (or particles) are typically assumed to be smaller than a grid cell. Practical applications however include situations where the mesh is comparatively fine, e.g. when meshing the wall boundary layer or in cases with growing bubbles. This may lead to non-convergent behaviour in mesh studies or to void fraction oscillations. To tackle this problem, a filtering approach is proposed, based on an additional diffusion term in the continuity equation. This approach increases the robustness of the results in regions of high spatial resolution, significantly reducing mesh-dependency of the simulation results. The implementation is straightforward, without a need to solve any additional system of equations. It is analysed in four different bubbly flow cases with varying characteristics: 2D/3D, wedge, square, and cuboid computational domains, with resolutions up to 32 cells per bubble diameter, laminar and turbulent flows, and several ways of gas injection. The additional computational effort varies, but is moderate. The proposed approach is applicable in multi-field two-fluid models for which a stable Euler-Euler behaviour on fine meshes is required, for example to prepare the transfer to an interface-resolving volume-of-fluid representation in morphology-adaptive approaches.

1. Introduction

The two-fluid model is typically applied in combination with closure forces designed for coarse grids, i.e. bubbles are typically assumed to be smaller than a grid cell (Tomiyama et al., 2003). If the spatial resolution is refined such that the grid cells become smaller than the bubble diameter under consideration, the model does not converge to the desired result. Unwanted phenomena like gas concentration or unphysical oscillations are observed. For example, Tomiyama et al. (2003) reported an unphysical accumulation of gas towards the pipe centre when he applied his well-known lift force formulation (Tomiyama, 2002) to a generic test problem. Comparable effects could also occur when simulating particle-laden flows, but the current work focuses on bubbly flows.

The following situations typically require to run a two-fluid model on a fine mesh:

- A simulation is repeated on finer meshes to proof that the results are independent with respect to spatial resolution (mesh studies).
- A local refinement is necessary to capture the flow field (e.g. boundary layers or vortices) and bubbles are transported into these mesh regions.
- Gas bubbles are generated (e.g. by boiling) or grow (due to pressure change, phase transfer or coalescence).

The latter aspect is of particular interest in the context of hybrid methods which conceptually allow that a bubble can be represented as disperse or continuous phase, depending on the local mesh size (Frederix et al., 2021; Meller et al., 2021; Colombo et al., 2022). Robust two-fluid results are crucial in order to capture the over-resolved state of disperse bubbles.

Two approaches are known to overcome this inconsistency:

- Number density transport (Tomiyama et al., 2003),
- Particle-centre averaging (Lyu et al., 2022).

Both concepts tackle the inconsistency problem by taking the bubble centre position into account. The former approach is based on a division

* Corresponding author.
E-mail address: b.krull@hzdr.de (B. Krull).

https://doi.org/10.1016/j.ces.2024.119909
Received 28 April 2023; Received in revised form 8 February 2024; Accepted 18 February 2024
Available online 23 February 2024

Table 1
HZDR baseline model for monodisperse bubbly flows (Hänsch et al., 2021).

Force and turbulence	Selected model
Drag force	Ishii and Zuber (1979)
Shear-lift force	Hessenkemper et al. (2021)
Turbulent dispersion force	Burns et al. (2004)
Wall-lift force	Hosokawa et al. (2002)
Virtual mass force	Constant coefficient (Auton et al., 1988)
Turbulence	k-ω SST (Menter, 2009)
Bubble-induced turbulence	Ma et al. (2017)

of cells into sub-cells and a numerical integration of the forces within these cells. The latter approach follows the same idea and incorporates forces which are consistent with the particle-centre averaged quantities. However, an existing code becomes quite complex in both cases and computational effort significantly increases.

Instead of aiming for a consistent solution to the inconsistency problem, the present work aims for a pragmatic stabilisation with low computational effort. The idea is to filter all volume fraction fields equally in order to mimic a coarser mesh. The given two-fluid model and the applied closure forces (representing interfacial momentum exchange) stay untouched. The concept to approach fine meshes with some sort of smoothing operation is also applied in the Euler-Lagrangian context (Pirker et al., 2011; Huang et al., 2023).

After describing the basic framework for implementation (Sec. 2) and the filtering approach (Sec. 3), four different test cases are presented: A basic test case with bubbles injected in an undisturbed uniform flow (Sec. 4), a second case with centred gas injection in a parabolic flow (Sec. 5), a pipe flow with near wall gas peaks (Sec. 6), and, finally, a bubble column driven by point mass sources (Sec. 7). These tests inspect the capability of the proposed method to reduced mesh dependence while applying the common closure forces.

2. Basic method

The procedure derived in the next section is publicly available in the Multiphase Code Repository by HZDR for OpenFOAM Foundation software (Schlegel et al., 2023). It is based on the *multiphaseEulerFoam* framework of the Foundation release of *OpenFOAM* and is available under GPL license. The phase-averaged Navier-Stokes equations (Drew and Passman, 1999) consist of a continuity and a momentum balance equation for each phase α:

$$\partial_t r_\alpha + \nabla\cdot\left(r_\alpha \mathbf{u}_\alpha\right) = 0, \tag{1}$$

$$\partial_t\left(r_\alpha \mathbf{u}_\alpha\right) + \nabla\cdot\left(r_\alpha \mathbf{u}_\alpha \mathbf{u}_\alpha\right) = -\frac{1}{\rho_\alpha} r_\alpha \nabla p + \nu_\alpha \nabla\cdot\left(2 r_\alpha \mathbf{S}_\alpha\right) + r_\alpha \mathbf{g} + \frac{1}{\rho_\alpha}\mathbf{f}_\alpha. \tag{2}$$

The phase-specific volume fraction, density, and viscosity are r_α, $\rho_\alpha = const$, and $\nu_\alpha = const$, respectively. The phase-averaged velocity vector is $\mathbf{u}_k$, p is the pressure, which is shared between all phases, and $\mathbf{g}$ denotes the vector of gravity. The phase-specific shear-rate tensor is $\mathbf{S}_\alpha = \frac{1}{2}\left(\nabla\mathbf{u}_\alpha^{\mathrm{T}} + \nabla\mathbf{u}_\alpha\right) - \frac{1}{3}\left(\nabla\cdot\mathbf{u}_\alpha\right)\mathbf{I}$. The vector of interfacial momentum exchange is referred to as $\mathbf{f}_\alpha$.

The equations are spatially discretised with a second order finite volume method and integrated in time with a semi-implicit Euler-scheme of first order accuracy. The pressure-velocity coupling is realised via PIMPLE algorithm (Greenshields and Weller, 2022). An interface compression term is applied to the phase-fraction transport equations (Weller, 2008).

3. Volume fraction filtering

The idea is to mimic a coarser mesh by applying a smoothing filter to the volume fraction. The strategy is as follows:

1. Identify a suitable Gaussian filter parameter σ.
2. Realise the filter as diffusion term in the continuity Eq. (1)

$$\partial_t r_\alpha + \nabla\cdot\left(r_\alpha \mathbf{u}_\alpha\right) = \nabla\cdot\left(C\nabla r_\alpha\right) \quad \text{with} \quad C = \min\left(C_{\mathrm{F}}, C_{\max}\right) \tag{3}$$

with the filter diffusion C_F computed from σ and limited by $C_{\max}$.

Mass conservation is ensured as the diffusion is applied to both phases with the same diffusion coefficient which preserves the volume fraction sum.

Related methods Note that this approach has to be distinguished from approaches filtering the whole set of the basic equations. Such considerations usually lead to closure terms scaling with the given mesh resolution, comparable with Large Eddy Simulations. Examples for this approach applied for gas-solid flows are reported in Milioli et al. (2013); Cloete et al. (2018); Schneiderbauer (2017). The goal of the present method however is not the derivation of specific terms, but to extend the applicability of an existing method. It starts from a model which produces plausible results on coarse meshes and tries to reproduce the same behaviour on meshes with much higher spatial resolution.

Identification of filter parameter σ The volume fraction r_α is defined as the filtered phase function X_α by

$$r_\alpha(\mathbf{x}) = \int_{\mathbb{R}^n} K(\mathbf{x}-\mathbf{y})\, X_\alpha(\mathbf{y})\, \mathrm{d}\mathbf{y} \tag{4}$$

for each phase α. We assume that the filter is represented by a Gaussian filter kernel

$$K(\mathbf{x}-\mathbf{y}) = \frac{1}{(2\pi\sigma^2)^{n/2}} e^{-\frac{||\mathbf{x}-\mathbf{y}||^2}{2\sigma^2}} \tag{5}$$

for a given number of dimensions n. In the limit $\sigma \to 0$, one obtains $r_\alpha \to X_\alpha$ which means that the filtering has no effect in this case. Let h be a measure for the local cell width of a given mesh, computed by the third root of the local cell volume, $h = \Delta V^{\frac{1}{3}}$. The goal is to apply a filtering on fine meshes with $d \gg h$ so that a coarse mesh is mimicked. For this purpose, the filtering should have an integrating effect at the order of the bubble diameter:

$$\sigma = K d. \tag{6}$$

The task is to identify K so that the filter has no measurable effect on coarse meshes with $d \le h$. This is done by setting $K = 1/m$ with $m \in \mathbb{N}$ and increasing m until there is no measurable difference between the unfiltered and the filtered field for the border case $d = h$ (up to machine precision). This procedure leads to $K = 1/8$ and hence to

$$\sigma = \frac{d}{8}. \tag{7}$$

With this choice, no filtering effect is measurable on coarse meshes with diameter resolutions $d/h \le 1$, but the filter becomes more and more active with growing diameter resolutions d/h. A decrease would cause the filter to be still inactive when needed and an increase of K would cause measurable filter effects on common Euler-Euler meshes with $d \le h$, which is unwanted. Some demonstration examples are presented in Table 2. By construction, the filtering effect becomes significant on fine meshes. The maximum relative deviations between the unfiltered and filtered fields for the resolutions $d/h \approx 3, 5, 28$ are 0.8%, 16.8%, 49.3%, respectively. With increasing grid resolution, the unfiltered grid void fraction converges towards the phase function. The filtered grid void fraction however converges consistently towards the analytically determined void fraction.

Filter-equivalent diffusion Applying the Gaussian filtering with parameter σ is equivalent to solving the diffusion equation with a given diffusion coefficient C for a time span τ (Bronshtein et al., 2015). This

Table 2
Void fraction for a given bubble of diameter d (black circle) for different spatial resolutions.

Mesh resolution	Void fraction on given grid (top), additional filter applied (bottom)	Void fraction and underlying phase function along horizontal centre line trough the domain shown on the left
9x9 cells $d/h \approx 3$ *filtering without effect on coarse mesh*	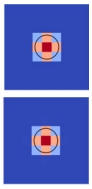	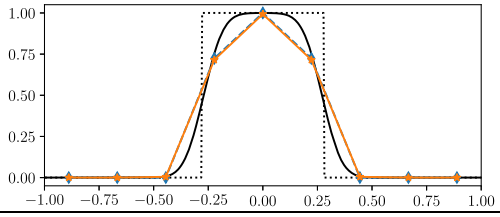
17x17 cells $d/h \approx 5$ *filtering with slight effect on intermediate mesh*		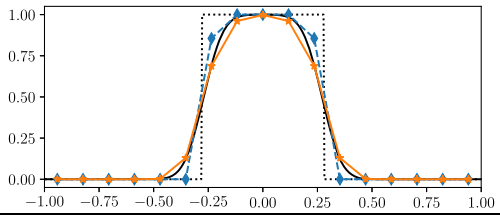
99x99 cells $d/h \approx 28$ *filtering with significant effect on fine mesh*	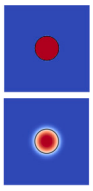	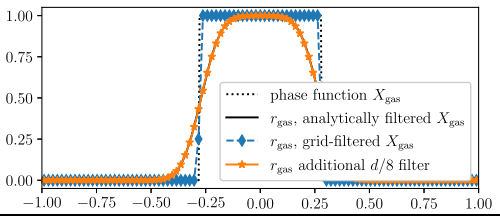

is reflected by the relation $\sigma^2 = 2C\tau$. The filter diffusion coefficient C_F is:

$$C_F = \frac{\sigma^2}{2\tau} = \frac{d^2}{128\tau}. \tag{8}$$

It is crucial that the diffusion time scale τ is chosen to be independent of the time step size Δt to make the filtering independent from the specific choice of the temporal resolution. However, the diffusion time scale should be close to Δt so that the desired filtering is realised in approximately one time step. Therefore, τ is chosen as $\tau = h/U$ based on a local characteristic velocity U defined as the largest velocity magnitude among all phases. This time scale is the characteristic time scale of the discrete convective transport and close to Δt because of the Courant number restriction. As a result, the diffusion coefficient scales with $\sim 1/h$, i.e. it is increased on fine meshes. Other possibilities to choose τ are discussed in Lyu et al. (2022).

Diffusion limiter The filter diffusion coefficient is limited by a maximum diffusion coefficient C_{max},

$$C = \min\left(C_F, C_{max}\right), \tag{9}$$

to obtain the following properties:

1. The convective transport of the volume fraction should always be possible and never be suppressed by the filter diffusion.
2. A small filter diffusion coefficient allows to add the diffusion term in an explicit manner. This keeps both implementation effort and computational cost low.

Limiting the diffusion coefficient reduces the filtering effect, which is acceptable to certain degree. To make sure that the convective transport of the volume fraction is always dominating a potential diffusion due to filtering, the filter diffusion coefficient is restricted by enforcing a minimal value for the mesh Péclet number $Pe = Uh/C$:

$$Pe_{min} \leq Pe \quad \Rightarrow \quad C_{max} = \frac{Uh}{Pe_{min}} \tag{10}$$

This upper diffusion limit scales with $\sim h$, i.e. the diffusion coefficient is more and more restricted with increased spatial resolution, approaching zero for extremely high diameter resolutions where switching to a volume-of-fluid method is definitely recommended. The lower mesh Péclet number limit Pe_{min} has to be chosen carefully. If chosen too small, the diffusion may still suppress the convective transport, which is not intended. If chosen too high, the filtering is basically switched off ($C \to 0$). Here, Pe_{min} is chosen to be $1/4$ which ensures sufficient convectional transport of the volume fraction.

An important stability criterion is the diffusion number $Di = C\Delta t/h^2$. It is relevant if the temporal discretisation of the diffusion term includes an explicit contribution. The limit for the one-dimensional fully explicit discretisation of the diffusion term is $Di \leq 1/2$. The above choice of the minimum mesh Péclet number implies an upper limit to the diffusion number: it imposes $Di \leq 4Co$ because of $Di = Co/Pe \leq Co/Pe_{min}$. This means that the formally required diffusion number limit could be violated in some cases. However, this condition is a sufficient stability criterion, not a necessary one. Going beyond this criterion does not necessarily mean that the method becomes unstable. For efficiency reasons, it is not strictly enforced in most cases (Ferziger and Perić, 2012). No explicit diffusion number limit is taken into account in the present work because the limit imposed by imposing a minimum mesh Péclet number is considered as sufficient. If required by future applications, the parameter Pe_{min} could be increased: this would result in less filtering diffusion, an earlier onset of the maximum clipping and a lower diffusion number. However, the choice of $Pe_{min} = 1/4$ turned out to be a suitable choice for the cases under consideration.

Complete expression The complete expression for the diffusion coefficient can be written as:

$$C = \frac{U}{h}\min\left(K_1 d^2, K_2 h^2\right) \tag{11}$$

or, expressed as a function of the bubble diameter resolution d/h, as

$$C = Ud\,\min\left(K_1\left(\frac{d}{h}\right), K_2\left(\frac{d}{h}\right)^{-1}\right), \tag{12}$$

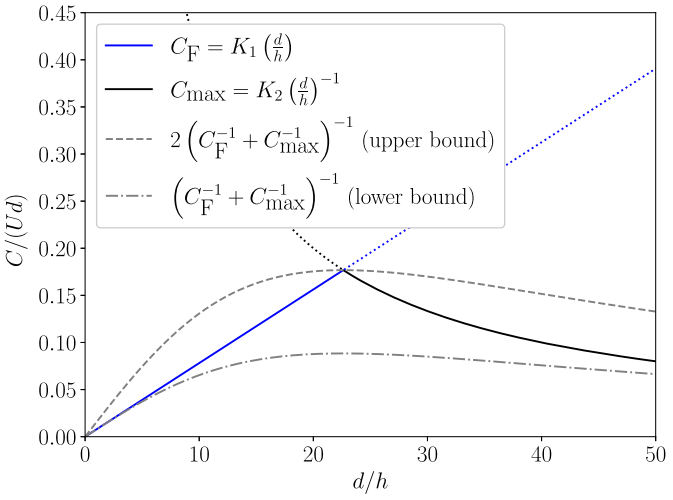

Fig. 1. Dependence of filter diffusion from bubble diameter resolution for $K_1 = 1/128$ and $K_2 = 4$, supplemented by smooth lower and upper bounds.

with the constants $K_1 = 1/128$ and $K_2 = Pe_{min}^{-1} = 4$. The behaviour of the filter coefficient C is sketched in Fig. 1. Both the lower and the upper bound of the effective (limited) diffusion are sketched in Fig. 1. The average of both is $1.5\left(C_F^{-1} + C_{max}^{-1}\right)^{-1}$ which could serve as a smooth replacement to Eq. (12), but is not applied here. The limiter gets active for diameter resolutions d/h larger than the critical value $\widehat{d/h} = \sqrt{128/Pe_{min}}$ which is approximately $\widehat{d/h} \approx 23$ for the given parameters (kink in Fig. 1). Because of the relation $K_2 = Pe_{min}^{-1} = \left(\widehat{d/h}\right)^2/128$, the choice of a minimum mesh Péclet number is equivalent to the choice of a certain critical diameter resolution determining the onset of the diffusion limiter. Note that C may vary in space, depending on the local representative diameter and the local characteristic velocity.

Solution procedure for volume of fluid method The finite volume multiphase formulation for the filter diffusion coefficient is

$$C = \frac{1}{2}\max_{\alpha}\left(\sum_f |\phi_{\alpha,f}|\right)\min\left(K_1\frac{d^2}{\Delta V}, K_2\frac{1}{\sum_f \frac{S_f}{||\Delta \mathbf{x}_f||}}\right), \tag{13}$$

with the filter constant $K_1 = 1/128$ and the limiter constant $K_2 = 1/Pe_{min} = 4$. The left factor is the local maximum of the cell face (f) flux sums determined over all phases (α). The right factor is a pure geometrical expression, where ΔV is the cell volume, S_f is the cell face area, and $||\Delta \mathbf{x}_f||$ is the cell centre difference. Formula (13) is obtained from Eq. (11) by replacing the terms U/h and h^2 with the finite volume equivalents

$$\frac{U}{h} \to \max_{\alpha}\left(\frac{1}{2\Delta V}\sum_f |\phi_{\alpha,f}|\right), \quad h^2 \to \frac{\Delta V}{\sum_f \frac{S_f}{||\Delta \mathbf{x}_f||}} \tag{14}$$

with the convective fluxes $\phi_{\alpha,f}$. These expressions are a consequence of the finite volume formulas for Courant number and diffusion number, respectively. The filtering is implemented as diffusive flux

$$-\lfloor C \rfloor_f \nabla_n r_\alpha \tag{15}$$

when solving the modified continuity equation (3), where $\lfloor C \rfloor_f$ describes the linearly face-interpolated value of C. These fluxes are added to the existing convective fluxes in an explicit manner when solving the modified continuity Eq. (3). Recall that this operation is applied to all phases to avoid the violation of mass conservation.

Remark on the risk of gradient overshoot on fine meshes High spatial resolutions allow gradient overshoots. This cannot occur on coarse meshes which are the typically chosen for TFM applications. Assume that a closure force is derived on the basis of the filter described above (Eqn. (4) together with the filter width chosen according to Eqn. (7)) and that this force is implemented to the two-fluid model in the usual manner, i.e. without any additional explicit filtering. On fine meshes, such a closure force may encounter much higher volume fraction gradients as expected. The reason is the following. The filtering described by Eqn. (4) and Eqn. (7) implies, that there is a theoretical maximum gradient:

$$||\nabla r_\alpha|| \leq \frac{8}{\sqrt{2\pi}d} \approx \frac{3}{d}. \tag{16}$$

This upper limit is automatically fulfilled on coarse meshes, because the mesh can produce a volume fraction gradient of $1/h$ at most (which is lower than $3/d$ for low spatial resolutions with $d < 3h$). Hence, no gradient overshoot can happen on coarse meshes. On fine meshes, however, gradients may become significantly higher than the theoretical maximum ($1/h$ exceeds $3/d$ for high spatial resolutions with $d > 3h$). As a consequence, forces based on the volume fraction gradient, such as turbulent dispersion (Burns et al., 2004) and solid phase pressure (Gidaspow and Ettehadieh, 1983), may be overestimated on fine meshes if no additional measure is taken.

Remark on hyperbolicity Some authors report that the hyperbolicity of the overall system is of fundamental importance to obtain meaningful results (Syamlal, 2011; Fox, 2019), some authors consider it to be too restrictive for the non-linear second order TFM equations (Thyagaraja and Fletcher, 1989), many authors do not take this property into consideration at all. An interesting stability analysis for the TFM is given by Stewart (1979): even if well-posedness (hyperbolicity) is not guaranteed, the TFM usually behaves well, provided the mesh is not too fine. The present work does not focus on hyperbolicity for the following reasons: A) The unphysical gas distributions on fine meshes reported in Tomiyama et al. (2003) are triggered by a lateral force, but lateral forces have no influence on hyperbolicity (Fox et al., 2020). Therefore, the potential lack of hyperbolicity cannot be the only explanation for such implausible results. B) The test described in Sec. 5, repeated with a hyperbolic closure taken from Panicker et al. (2018), still leads to unphysical results. C) The proposed approach mimics a coarser mesh which should avoid the growth of perturbations regardless of hyperbolicity (Stewart, 1979).

4. Gas injection in unhindered flow

All four presented cases (Sec. 4-7) feature air bubbles in water, covering different geometries and different bubble diameters in the range from 2.3 mm to 10 mm. The material properties applied are: $\rho_{gas} = 1.246\,kg\,m^{-3}$, $\rho_{liquid} = 999.7\,kg\,m^{-3}$, $\mu_{gas} = 1.84 \cdot 10^{-5}\,kg\,m^{-1}\,s^{-1}$, $\mu_{liquid} = 8.9 \cdot 10^{-4}\,kg\,m^{-1}\,s^{-1}$, $\sigma_{gas,liquid} = 0.072\,N\,m^{-1}$.

As a first test (Fig. 2), gas is injected in a vertical pipe with constant liquid velocity (uniform inflow with 1 m/s, free-slip walls to avoid wall effects). The pipe with a radius of $R = 20$ mm and a length of $L = 2R$ is modelled with a wedge geometry with 2.5°. The injected bubbles have a diameter of $d = R/5$. The injection into the free flow is applied at $r = R/2$ in a region of width d with a vertical extension of $(1/10)L \leq y \leq (3/20)L$. The wedge is resolved with one cell layer in the circumferentical direction, N cells over the radial and $2N$ cells in axial directions, respectively. The wedge is resolved using an uniform grid with N cells over the radial and $2N$ cells in axial direction, respectively.

The momentum closure terms (forces) are applied according to the baseline standard as listed in Table 1. Five refinement levels with factor 2 are applied, starting from $N = 10$ up to $N = 160$. The Courant number $Co = U\Delta t/h$ is kept below 0.4.

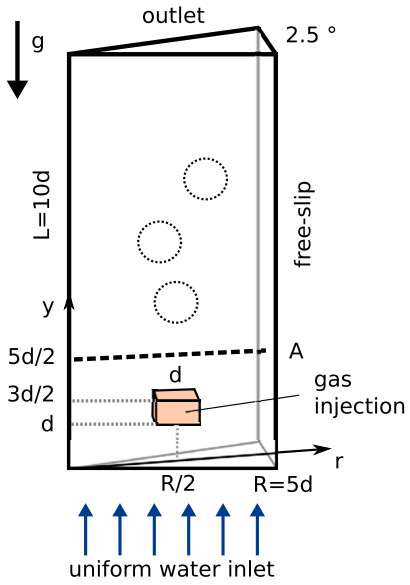

Fig. 2. Sketch of the computational domain for testing a box-shaped gas injection in unhindered flow.

A comparison is performed right after the injection region at a distance of one d (Fig. 3). The filtering procedure produces a consistent solution and, hence, a grid convergent behaviour is observed.

5. Vertical parabolic flow with centric gas injection

This test case features a gas injection in a fully developed parabolic liquid flow as reported in Lyu et al. (2022) motivated by Tomiyama et al. (2003).

The domain is a two-dimensional duct of width $W = 30\,\text{mm}$ and length $L = 500\,\text{mm}$ (Fig. 4). The bubbles are of size $d = 10\,\text{mm} = W/3$. The vertical upward liquid velocity is prescribed as a parabolic profile with $0.1\,\text{m/s}$ maximum in the centre and zero at both no-slip walls:

$$u_y = 0.1\left(1 - \left(\frac{2x}{W}\right)^2\right)\,\text{m/s}. \tag{17}$$

The origin of the Cartesian coordinate system is located in the centre of the pipe at the inlet boundary. The same profile is used to initialise the velocity field of both water and dispersed gas phases. The injection is realised by prescribing the void fraction field on the inlet as:

$$r_{\text{gas}} = \begin{cases} 0.005\left(1 - (2x/d)^2\right) & \text{, for } |x| \le d/2; \\ 0 & \text{, else.} \end{cases} \tag{18}$$

The domain is discretised with N cells in horizontal direction and $5N$ cells in the vertical direction, equidistant in each direction. The refinement levels for the comparison are achieved by doubling the number of cells in each direction, resulting in even values for N (Fig. 6). Additional refinement levels feature odd values for N so that raw centre values are available, without any interpolation potentially hiding oscillations (Fig. 5). Again, the time step size was adjusted so that the Courant number is kept below 0.4. The momentum closure terms (forces) are applied according to the baseline standard as listed in Table 1.

If the standard model is applied, i.e. the void fraction field is not filtered, the void fraction amplitude increases with each refinement step, which is unphysical (Figs. 5 and 6). Oscillations are observed on very fine meshes (Fig. 5). These oscillations correlate with the cell width and introduce a transient behaviour. Note that the peak values get even larger if the case is computed with a laminar setup (no turbulence model, no turbulent dispersion, no bubble-induced turbulence; not shown here). The turbulent dispersion plays a key role here, being responsible for the saturation of the centre amplitude visible in Fig. 5.

If the filtering is applied, the void fraction profiles are getting similar to the results on the coarse mesh (Fig. 6). The oscillations observed with the standard model disappear. Overall, the results in Fig. 6 are very similar to the results obtained with the particle-centre average method in Lyu et al. (2022), but obtained with less effort both in terms of implementation and computational resources.

6. Pipe flow with gas accumulation near wall

A vertical pipe flow with wall-near void fraction peaks is investigated. The selected case is taken from Liu (1989); Liu and Bankoff (1993a,b). It features a vertical flow through a pipe with a radius of $R = 19\,\text{mm}$ and a length of $L = 1\,\text{m}$ and is defined by the superficial velocities $J_{\text{gas}} = 0.027\,\text{m/s}$ and $J_{\text{liquid}} = 1.087\,\text{m/s}$. The numerical setup is published by Hänsch et al. (2022).

The pipe is modelled as wedge geometry with a wedge angle of 2.5°. The injected bubbles have a diameter of $d = 2.3\,\text{mm} \approx R/8$. The injection is applied by prescribing $r_{\text{gas}} = 2.42\%$ uniformly at the inlet with a uniform inlet velocity of $U_{\text{inlet}} = 1.114\,\text{m/s}$. The wedge is resolved with one cell layer in the circumferentical direction, N cells over the radial and $(18/5)N$ cells in axial direction, respectively. Again, the cell width is equidistant in each spatial direction and the momentum closure terms (forces) are applied according to the baseline standard as listed in Table 1. Five refinement levels with factor 2 are applied ranging from $N = 5$ to $N = 80$. The Courant number Co is kept below 0.4.

The Euler-Euler modelling of such cases is challenging, because the wall peaks of the void fraction profile are significantly over-predicted with the standard model. The model predicts a wall-near gas volume fraction peak of more than 0.2, which is more than twice the experimentally measured gas volume fraction wall-peak of approximately 0.08 (Fig. 7a, Fig. 7c). Even if the peak is not dampened for all spatial resolutions, the proposed filtering leads to improved results, which are qualitatively and quantitatively closer to the experimental data resulting in a very good agreement on the finest resolution with $d/h = 9.6$ (Fig. 7b, Fig. 7d). The proposed method helps to predict such wall peak situations, even if the results are not perfect yet, which indicates the need of further modelling work regarding the closure for wall-near bubble behaviour.

7. Bubble column

Bubble column cases are more complicated than pipe flows because a) the bubbles drive the liquid flow which makes predicting their correct behaviour much more important and b) numerical errors (artifacts, transients) stemming from initial conditions do not dissipate from the system through an outlet. Bubble columns are of industrial relevance and typically come with very different bubble sizes.

A generic case of a bubble column with large bubbles is investigated, featuring a monodisperse case with large bubbles (Fig. 8). The bubble column has a size of $(W, D, H) = (100, 40, 100)\,\text{mm}$ with bubbles of size $d = 5\,\text{mm}$, injected close to the bottom centre. To allow several refinement levels with moderate computational effort, only a quarter of a bubble column is simulated, i.e. the computation domain is of size $(W/2, D/2, H) = (50, 20, 100)\,\text{mm}$ with two symmetry boundaries.

The gas injection is realised by two point mass sources with a common mass flow rate of $3.552 \times 10^{-6}\,\text{kg/s}$. Both point mass sources are located at a distance of $(5+\varepsilon)\,\text{mm}$ from the large symmetry plane ($z = 0$) and at distances of $(5+\varepsilon)\,\text{mm}$ and $(15+\varepsilon)\,\text{mm}$ from the small symmetry plane ($x = W/2$). The offset $\varepsilon = 0.1\,\text{mm}$ is numerically motivated: it ensures that the point sources are never located at cell faces and never assigned to cells with direct contact to the symmetry boundaries. The side walls are no-slip walls, the top boundary allows slip and allows degassing. The degassing boundary condition replaces each gas fraction arriving in the uppermost cell layer with the corresponding amount of

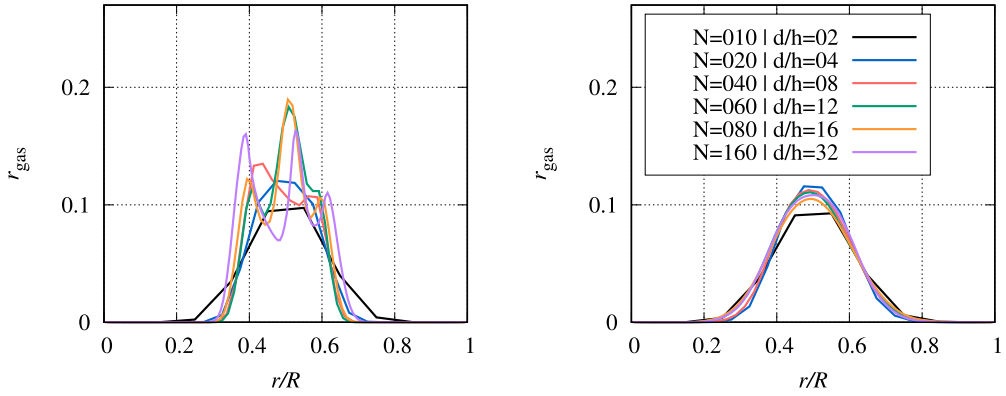

(a) No filtering applied. (b) Filtering applied.

Fig. 3. Gas volume fraction profile at a distance of one bubble diameter ($d = R/5$) above the injection region for different mesh resolutions.

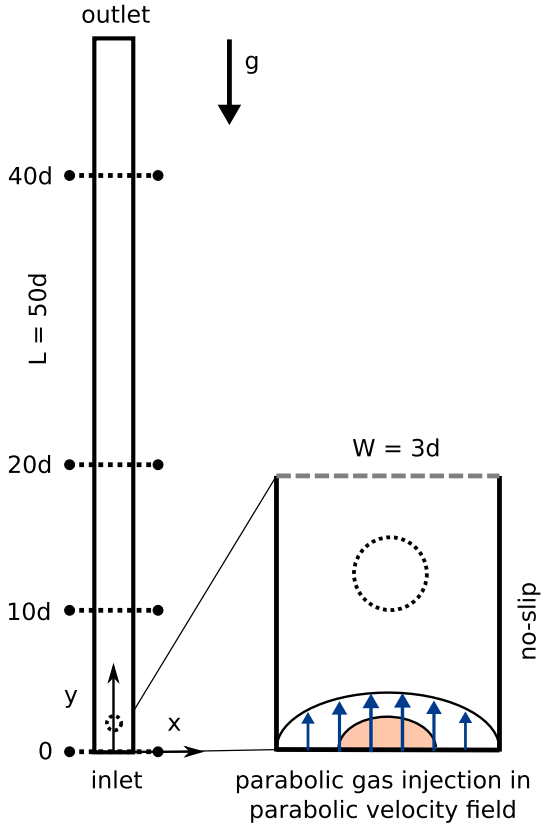

Fig. 4. Test case setup for parabolic gas injection in parabolic flow.

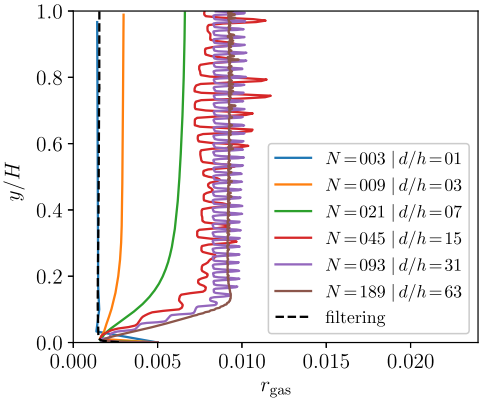

Fig. 5. Instantaneous void fraction values along vertical centre axis obtained with the standard model (no filtering). Oscillations are visible on the two finest resolutions. A filtered solution is shown as reference (finest mesh, dashed line).

water. The domain is resolved with N cubic cells in the lateral direction (x), $(2/5)N$ cells in depth direction (z), and $2N$ cells in the vertical direction, respectively. The cell size for the coarsest resolution with $N = 5$ is indicated on the bottom of the domain in Fig. 8. Five refinement levels with factor 2 are applied, the Courant number is kept below 0.4. The momentum closure terms (forces) are applied according to the baseline standard as listed in Table 1, except that the turbulent dispersion was excluded to obtain a stationary result for simpler comparison.

A slight over-resolution with $d = 2h$ is already enough to produce an increased gas volume fraction peak (Table 3, top row). For even higher diameter resolutions, a multi-peak gas volume fraction profile is observed, similar to the patterns found in the basic test case in Sec. 4. The filtering reduces the overshoot and aligns the solutions obtained on the fine meshes with a diameter resolution of 4 and 6 cells (Table 3, bottom row). The results obtained on the coarse mesh with $d \leq h$ are not disturbed by the filtering procedure.

8. Computational effort

For efficiency reasons, the authors decided to implement an explicit solution procedure, which directly adds the numerical fluxes resulting from filtering to the convective fluxes when solving the modified continuity equation, Eq. (3) (see Sec. 3). Tests showed that the alternative implementation as additional fractional sub-step would come with an increased effort of approximately +30% to +100% CPU time in the numerical context described in Sec. 2. Recall that the diffusion limiter is of fundamental importance for a stable explicit treatment, which means that the parameter $K_2 = 4$ has a direct influence on the computational effort.

The explicit realisation of the proposed filtering has the following impact on the computational effort: On coarse meshes, there is almost no additional computational cost, the solution procedure is carried out as usual. For slightly over-resolved cases with several cells per bubble diameter, a reduction of the computational time may be achieved. The effort increases in cases of very high diameter resolutions before it decreases again due to the diffusion limiter.

Some numbers are given for the considered cases, to get an impression. Note that these numbers reflect tendencies, because the cases have not been repeated often enough to rule out possible delays of the computational system. In the basic case (Sec. 4), the change with respect to computational time was in the order of −80% and +120% (average −40%) if compared to the computational time without filtering, i.e. the

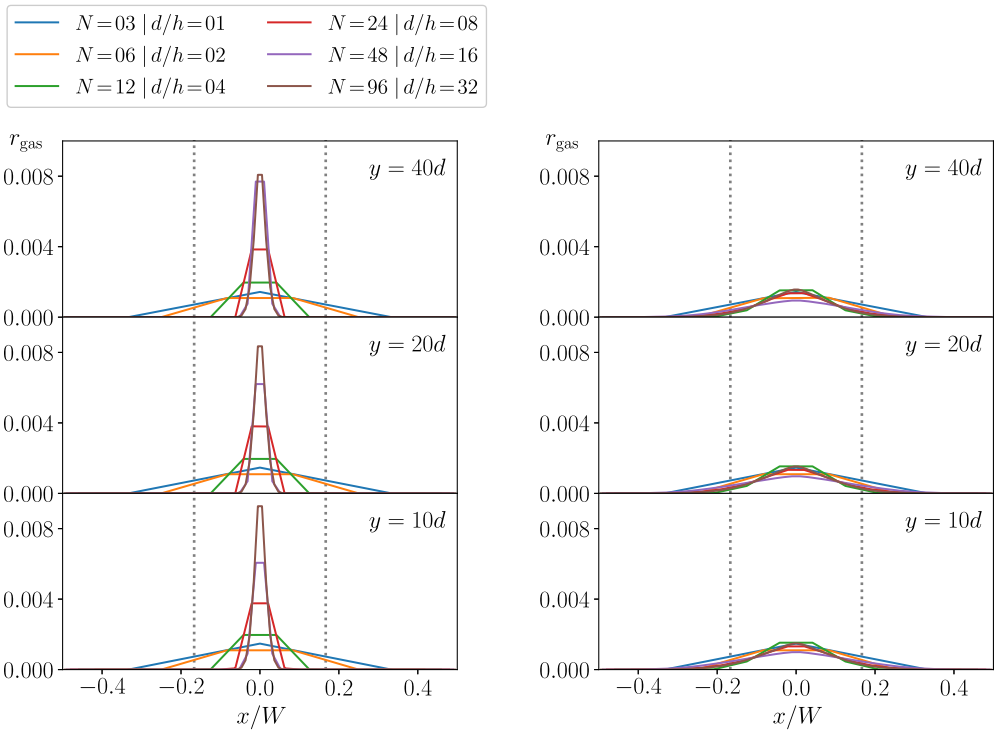

(a) No filter applied. (b) With filter applied.

Fig. 6. Gas volume fraction values along horizontal lines for three different vertical positions without and with filtering applied. The distance between the dashed lines is equal to the bubble diameter.

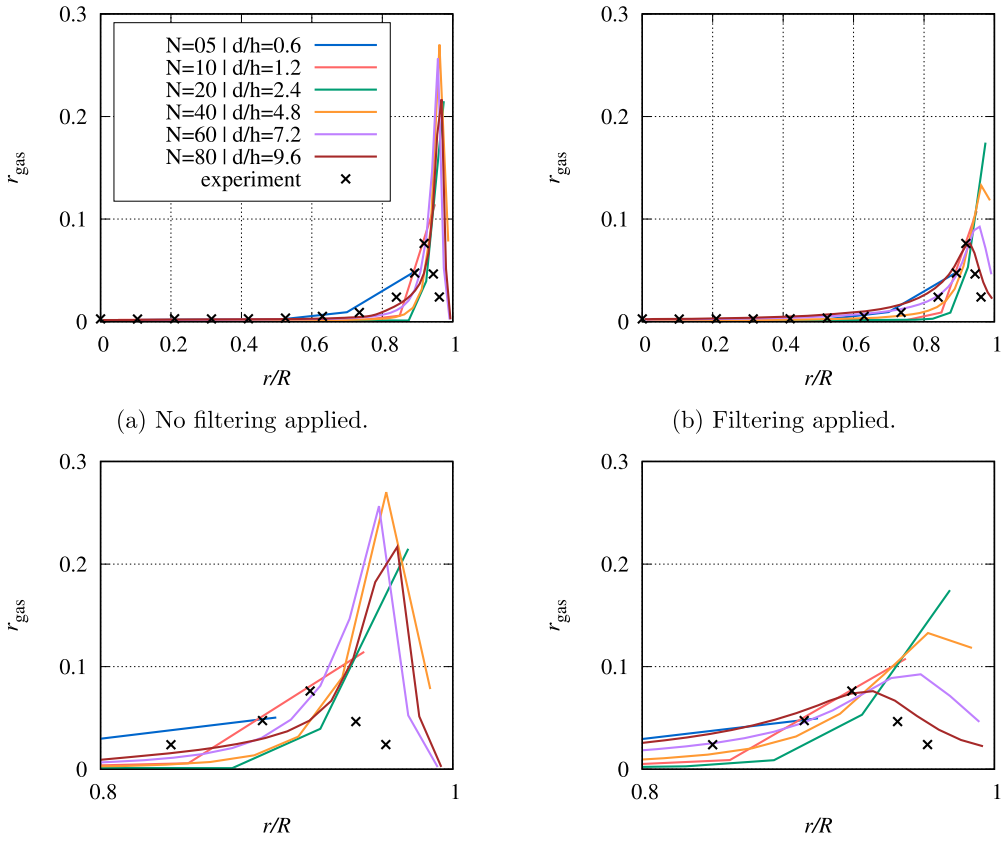

(a) No filtering applied. (b) Filtering applied.

(c) Zoom of (a). (d) Zoom of (b).

Fig. 7. Wall-peak behaviour at different refinement levels without and with filtering applied.

Table 3
Gas volume fraction along the lines A and B at height $y = 0.5H$ (see Fig. 8).

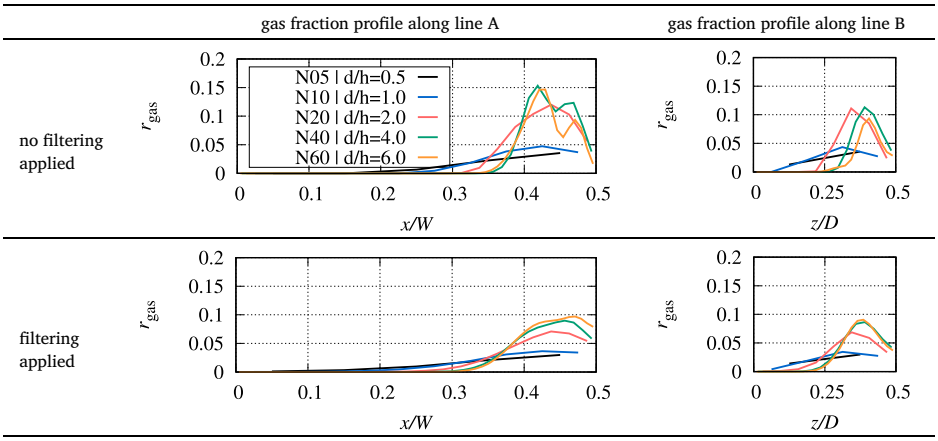

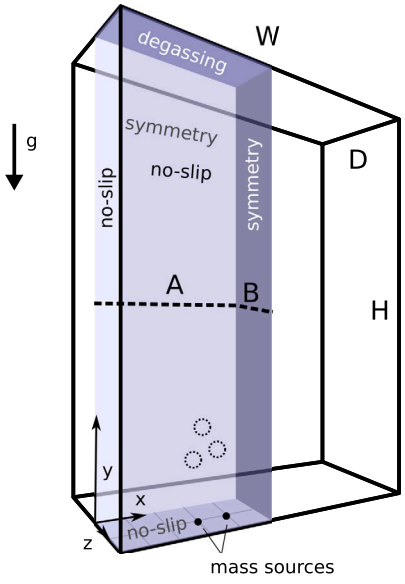

Fig. 8. Sketch of the bubble column (solid lines) and the computational domain (coloured). The back plane and the right plane are symmetry boundaries. The black dashed lines (A, B) are the lines chosen for extraction of line data for comparison. The coarsest grid with $N = 5$ is indicated at the bottom wall. The dashed spheres indicate the approximate bubble size.

results were improved and the computational effort was reduced on average. Fewer iterations were needed for the pressure-velocity coupling, possibly a consequence of weaker gradients. In the second case (Sec. 5), the change of the computational time depends strongly on the existence of the oscillations mentioned above: for the cases without oscillations, the computational time was about −40% and +80% (average +5%) in comparison to the computational time without filtering. The damping of the oscillations, however, causes significantly more computational effort (about +100% on the finest mesh). More detailed studies of these cases could provide information on how to improve closure models. In the third and fourth case (Sec. 6 and Sec. 7), the impact of the filtering on computational cost was between −20% and +60%, correlating with the height of the gas volume fraction peaks. Note that the values above were obtained on the same hardware, but not repeated several times, which is why they only reflect a tendency.

9. Conclusions

The standard Euler-Euler model and the corresponding closure forces are not designed to be applied on very fine meshes where the bubble diameter exceeds the local cell size. This may result in unphysical distributions of the disperse phase, even if hyperbolicity of the overall system is ensured. A volume fraction filtering approach is proposed to obtain more reliable results in these over-resolved cases. The approach suggests an additional diffusive term in the continuity equation (Eq. (3)) with a specific limited diffusion coefficient depending on the resolution of the bubble diameter. The diffusion term can be implemented explicitly, which comes with low implementation effort. There is no need to solve an additional system of equations. The impact of the procedure on the computational effort varies strongly depending on the physical problem and the spatial resolution. The maximum observed deviations from the standard computational time are −80% and +120% for specific cases, i.e. there are also cases where the present procedure saves computational cost. The method is applied to four different cases with different characteristics: 2D/3D, wedge, square, and cuboid domain geometry, laminar and turbulent flow, various gas injection methods (cell set in free flow, uniform and non-uniform inlet profiles, point mass sources), and diameter resolutions up to 32 cells per diameter. The method allows a sufficiently reliable behaviour of the Euler-Euler models, even if the diffusion is slightly too strong or slightly too high for some intermediate resolutions. For the Euler-Euler method in consideration, the mesh dependence of the results was significantly decreased. This paves the way for simulations of complex practical problems with local mesh refinement, for polydisperse cases with various bubble sizes, or particle-laden flows, which may all be subject of future endeavours. The procedure can be incorporated in morphology-adaptive methods to ensure a consistent behaviour for over-resolved Euler-Euler situations (as the counter-part to the under-resolved volume-of-fluid scenarios addressed in Meller et al. (2023)).

CRediT authorship contribution statement

Benjamin Krull: Conceptualization, Formal analysis, Investigation, Methodology, Software, Visualization, Writing – original draft, Writing – review & editing. **Richard Meller:** Conceptualization, Formal analysis, Investigation, Methodology, Software, Writing – review & editing. **Matej Tekavčič:** Methodology, Software, Writing – review & editing. **Fabian Schlegel:** Conceptualization, Funding acquisition, Investigation, Methodology, Project administration, Resources, Software, Supervision, Writing – review & editing.

Declaration of competing interest

The authors declare that they have no known competing financial interests or personal relationships that could have appeared to influence the work reported in this paper.

Data availability

Data will be made available on request.

Acknowledgements

This work was partly supported by the Helmholtz European Partnering Program in the project *Crossing borders and scales (Crossing)*. The authors gratefully acknowledge the financial support provided by the Slovenian Research and Innovation Agency through grant P2-0026.

References

Auton, T.R., Hunt, J.C.R., Prud'Homme, M., 1988. The force exerted on a body in inviscid unsteady non-uniform rotational flow. J. Fluid Mech. 197, 241–257.

Bronshtein, I., Semendyayev, K., Musiol, G., Mühlig, H., 2015. Handbook of Mathematics. Springer Berlin Heidelberg.

Burns, A., Frank, T., Hamill, I., Shi, J.-M., 2004. The Favre averaged drag model for turbulent dispersion in Eulerian multi-phase flows. In: 5th International Conference on Multiphase Flow. ICMF'04, Yokohama, Japan, May 30-June 4, 2004, 392.

Cloete, J.H., Cloete, S., Municchi, F., Radl, S., Amini, S., 2018. Development and verification of anisotropic drag closures for filtered two fluid models. Chem. Eng. Sci. 192, 930–954. https://doi.org/10.1016/j.ces.2018.06.041.

Colombo, M., De Santis, A., Hanson, B., Fairweather, M., 2022. A Generalized Multifluid Modelling Approach (GEMMA): application to multiple flow regime phenomena in nuclear reactor thermal hydraulics. In: Proceedings of NURETH-19.

Drew, D., Passman, S., 1999. Theory of Multicomponent Fluids, vol. 135. Springer-Verlag, New York. ISBN 978-1-4684-9227-9.

Ferziger, J.H., Perić, M., 2012. Computational Methods for Fluid Dynamics. Springer Science & Business Media. ISBN 3-540-42074-6.

Fox, R.O., 2019. A kinetic-based hyperbolic two-fluid model for binary hard-sphere mixtures. J. Fluid Mech. (ISSN 1469-7645) 877, 282–329. https://doi.org/10.1017/jfm.2019.608.

Fox, R.O., Laurent, F., Vié, A., 2020. A hyperbolic two-fluid model for compressible flows with arbitrary material-density ratios. J. Fluid Mech. (ISSN 1469-7645) 903. https://doi.org/10.1017/jfm.2020.615.

Frederix, E.M.A., Dovizio, D., Mathur, A., Komen, E.M.J., 2021. All-regime two-phase flow modeling using a novel four-field large interface simulation approach. Int. J. Multiph. Flow 145, 103822. https://doi.org/10.1016/j.ijmultiphaseflow.2021.103822.

Gidaspow, D., Ettehadieh, B., 1983. Fluidization in two-dimensional beds with a jet. 2. Hydrodynamic modeling. Ind. Eng. Chem. Fundam. 22 (2), 193–201. https://doi.org/10.1021/i100010a008.

Greenshields, C., Weller, H., 2022. Notes on Computational Fluid Dynamics: General Principles. CFD Direct Ltd, Reading, UK.

Hänsch, S., Evdokimov, I., Schlegel, F., Lucas, D., 2021. A workflow for the sustainable development of closure models for bubbly flows. Chem. Eng. Sci. 244, 116807. https://doi.org/10.1016/j.ces.2021.116807.

Hänsch, S., Draw, M., Evdokimov, I., Khan, H., Krull, B., Lehnigk, R., Liao, Y., Lyu, H., Meller, R., Schlegel, F., Tekavčič, M., 2022. Multiphase case collection by HZDR for OpenFOAM foundation software. https://doi.org/10.14278/rodare.811.

Hessenkemper, H., Ziegenhein, T., Rzehak, R., Lucas, D., Tomiyama, A., 2021. Lift force coefficient of ellipsoidal single bubbles in water. Int. J. Multiph. Flow, 103587. https://doi.org/10.1016/j.ijmultiphaseflow.2021.103587.

Hosokawa, S., Tomiyama, A., Misaki, S., Hamada, T., 2002. Lateral migration of single bubbles due to the presence of wall. In: Proc. ASME Joint U.S.-European Fluids Engineering Division Conference (FEDSM2002). Montreal, Quebec, Canada. In: ASME Conf. Proc. 2002 Vol. 1: Fora, Parts A and B, p. 855.

Huang, C.-C., van Oijen, J.A., Deen, N.G., Tang, Y., 2023. A particle-size dependent smoothing scheme for polydisperse Euler-Lagrange simulations. Chem. Eng. Sci. 277, 118765. https://doi.org/10.1016/j.ces.2023.118765.

Ishii, M., Zuber, N., 1979. Drag coefficient and relative velocity in bubbly, droplet or particulate flows. Alchem. J. 25 (5), 843–855.

Liu, T.J., 1989. Experimental Investigation of Turbulence Structure in Two-Phase Bubbly Flow. PhD thesis. Northwestern Univ., Evanston, Illinois.

Liu, T.J., Bankoff, S.G., 1993a. Structure of air-water bubbly flow in a vertical pipe. I: liquid mean velocity and turbulence measurements. J. Heat Transf. 36, 1049–1060.

Liu, T.J., Bankoff, S.G., 1993b. Structure of air-water bubbly flow in a vertical pipe. II: void fraction, bubble velocity and bubble size distribution. J. Heat Transf. 36, 1061–1972.

Lyu, H., Lucas, D., Rzehak, R., Schlegel, F., 2022. A particle-center-averaged Euler-Euler model for monodisperse bubbly flows. Chem. Eng. Sci. 260, 117943. https://doi.org/10.1016/j.ces.2022.117943.

Ma, T., Santarelli, C., Ziegenhein, T., Lucas, D., Fröhlich, J., 2017. Direct numerical simulation–based Reynolds-averaged closure for bubble-induced turbulence. Phys. Rev. Fluids (ISSN 2469-990X) 2 (3). https://doi.org/10.1103/PhysRevFluids.2.034301.

Meller, R., Schlegel, F., Lucas, D., 2021. Basic verification of a numerical framework applied to a morphology adaptive multi-field two-fluid model considering bubble motions. Int. J. Numer. Methods Fluids 93 (3), 748–773. https://doi.org/10.1002/fld.4907.

Meller, R., Tekavčič, M., Krull, B., Schlegel, F., 2023. Momentum exchange modeling for coarsely resolved interfaces in a multifield two-fluid model. Int. J. Numer. Methods Fluids, 1–25. https://doi.org/10.1002/fld.5215.

Menter, F.R., 2009. Review of the shear-stress transport turbulence model experience from an industrial perspective. Int. J. Comput. Fluid Dyn. 23, 305–316.

Milioli, C.C., Milioli, F.E., Holloway, W., Agrawal, K., Sundaresan, S., 2013. Filtered two-fluid models of fluidized gas-particle flows: new constitutive relations. AIChE J. (ISSN 1547-5905) 59 (9), 3265–3275. https://doi.org/10.1002/aic.14130.

Panicker, N., Passalacqua, A., Fox, R., 2018. On the hyperbolicity of the two-fluid model for gas–liquid bubbly flows. Appl. Math. Model. (ISSN 0307-904X) 57, 432–447. https://doi.org/10.1016/j.apm.2018.01.011.

Pirker, S., Kahrimanovic, D., Goniva, C., 2011. Improving the applicability of discrete phase simulations by smoothening their exchange fields. Appl. Math. Model. 35 (5), 2479–2488. https://doi.org/10.1016/j.apm.2010.11.066.

Schlegel, F., Bilde, K.G., Draw, M., Evdokimov, I., Hänsch, S., Kamble, V.V., Khan, H., Krull, B., Lehnigk, R., Li, J., Lyu, H., Meller, R., Petelin, G., Kota, S.P., Tekavcic, M., 2023. Multiphase code repository by HZDR for OpenFOAM foundation software. https://doi.org/10.14278/rodare.767.

Schneiderbauer, S., 2017. A spatially-averaged two-fluid model for dense large-scale gas-solid flows. AIChE J. 63 (8), 3544–3562. https://doi.org/10.1002/aic.15684.

Stewart, H.B., 1979. Stability of two-phase flow calculation using two-fluid models. J. Comput. Phys. 33, 259.

Syamlal, M., 2011. A hyperbolic model for fluid–solids two-phase flow. Chem. Eng. Sci. (ISSN 0009-2509) 66 (19), 4421–4425. https://doi.org/10.1016/j.ces.2011.02.051.

Thyagaraja, A., Fletcher, D.F., 1989. The nonhyperbolicity of multiphase flow equations: a nonlinear nonproblem? Comput. Phys. Commun. 56, 115.

Tomiyama, A., 2002. Single bubbles in stagnant liquids and in linear shear flows. In: Workshop on Measurement Techniques for Steady and Transient Multiphase Flows.

Tomiyama, A., Shimada, N., Asano, H., 2003. Application of number density transport equation for the recovery of consistency in multi-field model. In: Proceedings of ASME FEDSM'03, 4th ASME_JSME Joint Fluids Engineering Conference. Honolulu, Hawaii, USA, July 6-10, 2003, Honolulu, Hawaii, USA.

Weller, H., 2008. A new approach to VOF-based interface capturing methods for incompressible and compressible flow. Technical Report 4. OpenCFD Ltd. TR/HGW/04.